Electronic Supplementary Material (ESI) for Physical Chemistry Chemical Physics.
This journal is © the Owner Societies 2019

Supporting information for "Towards infinite polarization retention in thin-film small-molecular organic ferroelectrics"

*Indre Urbanaviciute, Subham Bhattacharjee, Michal Biler, Jody A. M. Lugger, Tim D. Cornelissen, Patrick Norman, Mathieu Linares, Rint P. Sijbesma, Martijn Kemerink**

Contents

I. Synthetic procedures

BTA-C6/2

To an ice-cold solution of 1,3,5-Benzenetricarbonyl trichloride (1 equiv.) in dry DCM, 2-Ethyl-1-hexylamine (3.3 equiv.) was added at a time followed by addition of triethylamine (3.3 equiv.). The reaction mixture was stirred at room temperature for 16 h. After completion of the reaction, the solvent was dried. The crude product was dissolved in $CHCl_3$, which was washed with 1 M HCl solution twice before drying under vacuum. The crude product was purified by silica gel column chromatography using 1–3% MeOH in $CHCl_3$ as a solvent followed by recrystallization in acetone, which afforded pure BTA-C6/2 in 45% yield.

BTA-C7/6

To an ice-cold solution of 1,3,5-Benzenetricarbonyl trichloride (1 equiv.) in dry DCM, tridecan-7-amine (3.4 equiv.) was added at a time followed by addition of triethylamine (3.3 equiv.). The reaction mixture was stirred at room temperature for 12 h. After completion of the reaction, the solvent was dried. The crude product was dissolved in $CHCl_3$, which were washed with 1M HCl solution twice before drying under vacuum. The crude product was purified by silica gel column chromatography using $CHCl_3$ as a solvent followed by recrystallization in acetone, which afforded pure BTA-C7/6 in 40% yield. ^{1}H-NMR ($CDCl_3$, 400 MHz): $\delta = 8.38$ (s, 3H, Ar-*H*), 6.15 (br., 3H, N-*H*), 4.15 (m, 3H, C*H*), 1.26-1.61 (m, 60H, CH_2), 0.86 (t, 18H, CH_3). ^{13}C NMR (100 MHz, $CDCl_3$, 25 °C, TMS): $\delta = 14.05$, 22.61, 26.02, 29.24, 31.74, 35.42, 50.45, 127.80, 135.20, 165.12. ATR FT-IR (Neat, cm^{-1}): 3224, 3062, 2925, 2856, 1630, 1551, 1455, 1313, 1129, 954, 902, 795, 724, 692; Maldi-Tof MS: *m/z* calculated for $C_{48}H_{87}N_3O_3$ $(M+Na)^+$: 776.67, found: 776.59.

II. Device fabrication and conditioning

Thin film metal-ferroelectric-metal (MFM) capacitor devices for all probed materials were formed by spin-coating (700–1500 rpm) of a 40 mg/ml (15 mg/ml for BTA-C6/2 due to a low gel point) chloroform solution on a chemically cleaned glass substrate with patterned aluminum bottom electrodes. Before thermal vacuum deposition of the aluminum top electrodes, spin-coated films were annealed at 70 °C for 15 min to completely evaporate the solvent. The prepared MFM devices were 0.01–1 mm^2 in area. Typical film thickness was 300–800 nm, as measured by a Bruker Dektak XT profilometer.

In the as-cast organic ferroelectric film molecular columns lie in-plane to the electrode[1]. When molecular dipoles are oriented in this way, no polarization can be measured in the bottom-top electrode geometry. Therefore, prior to the electrical measurements the devices are treated by a field annealing procedure,[2,3] when at low viscosity conditions (≈70–100 °C) with the help of an alternating external field molecular bundles are forced to stand perpendicularly to the electrodes. The procedure takes ≈10–180 seconds (see Fig. S0), and accelerates with the applied field, its frequency and temperature. The followed field cooling freezes the system in this quasi-orderly state. Due to π-stacking of the benzene core and hydrogen bonding of the amide groups, accompanied by alkyl chain freezing, the hexagonal packing remains stable even without external field. This has been previously tested by polarized light optical microscopy (POM) and can be seen from unchanged current transients corresponding to polarization reversal after a long waiting time.[4] Therefore only the polarization switching current, rising from the dipole rotation, reflects in the quasi-statically measured *P-E* curves (see Electrical characterization), once the device is properly conditioned.

III. Electrical characterization

The polarization loops are obtained by integration of the switching current transients. We use a quasi-static mode, better known as the Double Wave Method (DWM),[5] when non-switching current is subtracted from the initial signal to avoid displacement and leakage inputs in the *P-E* curves. The input signal waveform is supplied by a Tektronix AFG3000 Arbitrary Function Generator and is amplified by a TREK PZD350A high voltage amplifier. The device response is visualized by a Tektronix TBS1000B Digital Oscilloscope.

The polarization retention measurement is performed using a similar DWM approach with a delay between the poling and probing signals. The devices are left at short circuit conditions during the waiting time. Each data point is measured after full repolarization. The device is considered depolarized when full polarization randomization is reached.

Switching kinetics is obtained from a step response measurement. The device is fully negatively poled and transient switching current is measured as a response to a positive square input signal of a different amplitude.[5]

IV. Other characterization

The surface topography of spin-coated BTA films has been studied by Veeco Dimension 3100 atomic force microscope in tapping mode.

Differential scanning calorimetry (DSC) studies were carried out in hermetic T-zero aluminum sample pans using a TA Instruments Q2000 – 1037 DSC equipped with a RCS90 cooling accessory. The thermal transitions were studied on the first cooling and second heating with the rate of 10 °C/min.

X-ray diffraction (XRD) studies were conducted using a Ganesha lab instrument equipped with a GeniXCu ultralow divergence source producing X-ray photons with a wavelength of 1.54 Å and a flux of 1×10^8 photons/second. Diffraction patterns were collected on a Pilatus 300 K silicon pixel detector with 487×619 pixels of 172 μm^2 in size. Glass capillaries were filled with the material for the diffraction analysis and placed in a Linkam HFSX350 heating stage and measured at a range of –25 °C to +250 °C with 10 °C/min. Each pattern was recorded for 10 min. Azimuthal integration of the obtained diffraction patterns was performed by utilizing the SAXSGUI software.

V. The behavior of BTA-C7/6 above 90°C

As mentioned in the main text, differently to all other homologues, polarization in **BTA-C7/6** is lost rapidly above 80°C and almost immediately after exceeding 95°C, even though the material is still in the plastic-crystalline state (ColHex ~120°C, melting temperature ~236°C). There is however a small peak in the DSC diagram at 95°C (Fig. S1d). As no change in packing fashion is seen from the WAXS results at around 95°C (Fig. S2c), this likely indicates changes in the tail mobility. Branched alkanes are known to have lower boiling point due to less condensed packing. If these branched **C7/6** alkyl tails become highly mobile at elevated temperatures, this might influence the strength of intermolecular hydrogen bonds, as the electrostatic bonding energy of ~0.75 eV (stabilization energy for stacks longer than a decamer)[6] could be overcome in this way. This could manifest itself as a double-peak in the switching current response to a triangular pulse, see Fig. S5a. Alternatively, this can be seen in small-signal capacitance vs. voltage and loss tangent characteristics (Fig. S5c,d) that show double-peak features and strong relaxation at small applied voltage range. The two depolarization processes with different rates, that can be distinguished from the depolarization kinetics above 90°C in Fig. 4b, further suggest the coexistence of two phases/conformations at and above this transitional temperature. Below that, **BTA-C7/6** behaves as a regular ferroelectric (Fig. S5 b–d)

VI. DFT/MD simulations

Computational Details

All molecules were optimized within the DFT formalism using the Gaussian software package[7]; the Ante_R.E.D. program[8–10] with B3LYP/cc-pVDZ was used to calculate ESP charges; topology and initial coordinate files were generated by the LEaP program with general amber force field (GAFF).[11] The system was first minimized to find the appropriate box size in *z*-direction, and then, it ran for 10 ns in NVT ensemble at 300 K using Langevin dynamics. At this point, the van der Waals and electrostatic energies were extracted. Then we applied the electric field, and we let the MD simulations run in NVT ensemble at 300 K for about 70 ns with a time step of 2 fs; simulations for boxes with 16 molecules ran for 80 ns. The trajectories were recorded every 5000 steps and the cut-off was set to 12 Å for non-bonded interactions. All MD simulations were carried out using either Amber 14 or Amber 16.[12,13]

As discussed in the main text, we constructed BTA self-assemblies for the model system **BTA-C1** (methyl tails) made of 22 BTA molecules in order to have a 3:0 rotamer. We built assembly of 22 molecules in 3:0 configuration for **C8**, and of 24 molecules in 3:0 configuration for **C12**, **C6/2(Rac)** and **C7/6(Rac)**. The racemic mixtures were built in the following order: the first molecule in *R-R-R* configuration followed by a molecule in *R-R-S*, *R-S-S*, and *S-S-S* configurations; this repeats six times to build the stack of 24 molecules to ensure the PBC.

We performed a simultaneous scan of three dihedral angles φ1, φ2, and φ3 (Fig. S7b) of a dimer in 3:0 configuration at B3LYP-D3/cc-pVDZ level of theory in order to obtain the energy barrier between the P- and M-helicities. The calculations were performed in vacuum with the Gaussian software package.

Model system BTA-C1 (methyl tail)

Conformers

We constructed a BTA self-assembly made of 22 BTA molecules to have a 3:0 rotamer (with minimized distance between BTA molecules being 3.316 Å). 22 BTAs were chosen to be able to apply periodic boundary conditions (PBC), and since the BTAs are twisted about 60° with respect to each other to keep the hydrogen bond network, the number has to be a multiple of two for 3:0 conformation. The conformer 3:0 was found to be the most stable and dominant after the application of the electric field, therefore studies of other possible conformers, e.g. 2:1, were left out of the scope of this article. Although our simulations started from P-helical BTA H-network conformation (clockwise, where BTA helicity is right-handed to form hydrogen bonds with the residues under and above), assemblies may adopt both P- or M-helicity (anti-clockwise with left-handed helicity), see Fig. S7a.

Effect of the field

In order to study the effect of an external electric field (E), we applied a series of electric fields with different strengths (0.001, 0.01, 0.035, 0.065, 0.11, 0.22, 0.28, 0.36, 0.43, and 1.0 V/nm) in both (+) and (−) directions with respect to the z-axis. The electric field value at which the flip of the dihedral angle was observed is further called a critical field. We chose three dihedral angles to follow the conformations, namely, dihedral angle 6-1-7-8 (φ1), 2-3-9-10 (φ2), and 4-5-11-12 (φ3) (Fig. S7b). At the very beginning of the MD simulations, all C=O and N-H moieties pointed below and above the plane, respectively, with dihedral angles being around 30° (Fig. S7a,c) for 3:0 rotamer in P-conformation. External electric field applied in the (+)-direction had no effect on the assembly as the system remained in the 3:0 orientation, whereas the (−)-direction of E switched the orientation from 3:0 to 0:3 rotamer. Indeed, after applying $E = 0.22$ V/nm, dihedral angles switched from around 30° to −30° (Fig. S7c). All C=O moieties switched at the same moment. This resulted in the helicity change of the hydrogen network from P to M, see Fig. S7d.[14] A helicity-maintaining full 180° flip is energetically unfavorable, therefore 60° flip is dominant. Electric fields below the critical field (< 0.11 V/nm) had no significant effect on the dihedral angles.

Inter-ring distance during the switch

For the 3:0 conformer dimer, we performed a scan at the QM level to determine the activation barrier to switch from M to P by flipping the amide moiety in a synchronized fashion through a planar conformation with respect to the phenyl group. The activation barrier was found to be around 6 kcal/mol, which is the energy cost for the simultaneous rotation of all six amides of both BTAs (Fig. S8). During this process, the two rings get closer to each other, with a decrease of the distance from 3.326 Å for the P and M conformers to 3.310 Å for the transition state corresponding to decrease of 0.6 %. This significant change in the interdisc distance with dipole switching is allowed due to moderate π-π interactions between small benzene cores. The remnant interdisc distance is expected to decrease with increasing number of monomer units[15].

BTAs with longer tails

Based on our **BTA-C1** model, we further examined BTA homologues with longer linear and branched achiral mesogenic tails. Following the experimental results, linear **BTA-C8** and **C12** together with branched **BTA-C6/2** and **C7/6** molecules were studied. The branched-tailed **C6/2** and **C7/6** materials were used as racemic mixtures in simulations. The mixture of *R*- and *S*-configurations was built in the following order: *R*-*R*-*R*, *R*-*R*-*S*, *R*-*S*-*S*, and *S*-*S*-*S*; this sequence repeated six times to build the stack of 24 molecules to ensure the PBC.

Influence of the chains on the packing

To study the effect of the substitutions on the packing, we performed a series of simulations on boxes made of 9 stacks for **C8**, **C12**, **C6/2**, and **C7/6**. Those initial boxes were then relaxed in an NPT ensemble (see examples in Fig. S9). To calculate the inter-stack distances and angles, we projected 100 frames (1 ns of MD simulation) of mass centers of benzene cores into the *xy* plane (Fig. S10). The results are summarized in Table S2. Columnar hexagonal packing of molecular columns was found for all materials. The intercolumnar distances obtained are in good agreement with the experimental X-ray scattering data, *vide supra*[1].

VII. Tables

Table S1. Fitting parameters used to fit the coercive field versus temperature trends with the thermally-activated nucleation-limited switching model.

	V^*, nm^3 *	w_b, eV/nm^3	E_{c0}, V/µm
BTA-C6; steep-slope	1	0.7	1970
BTA-C6/2; steep-slope	3.3	0.25	1140
BTA-C7/6; steep-slope	2.3	0.4	1650
BTA-C6; slight-slope	6.4	0.14	415
BTA-C6/2; slight-slope	8.7	0.12	525
BTA-C7/6; slight-slope	NA	NA	NA

* A constant attempt frequency was used for fitting. The extracted critical volume V^* value might therefore have a hidden attempt frequency dependence, as the slope of the characteristics is defined as ~ln(v_0)/V^*.

Table S2. Geometrically expected and experimentally obtained remnant polarization values for branched-tailed, linear BTAs and mixtures of the two. Experimental intercolumnar distance (Exp. *a*) was measured by small angle X-ray scattering technique at 80°C for pure materials, theoretical values (Theor. *a*, nm) were simulated by DFT/MD calculations.

	Material	Exp. *a*, nm*	Theor. *a*, nm	Geometrically expected P_r, mC/m^2	Experimentally obtained P_r, mC/m^2
Branched	BTA-C6/2	1.73	1.8	45	35
	BTA-C7/6	2.02	2.14	34	34
Linear	BTA-C6	1.55	-	57	55
	BTA-C8	1.72	1.78	47	45
	BTA-C12	2.08	2.20	32	32
Mixed	BTA-C8:C6/2, 1:1	1.73	-	45	42
	BTA-C12:C6/2, 1:1	2.08	-	32	36
	BTA-C12:C7/6, 1:1	2.08	-	32	33

* Intercolumnar distance of the linear-branched mixtures is assumed to be governed by the longer tail.

Table S3. Switching initialization time in nanoseconds at different strengths of applied electric field for isolated stacks from two independent simulations (separated by a semicolon). Duration of the switching process is given in brackets (the total switching time is the sum of the two). n.s. – no switching, s. – immediate switching.

E **(V/nm)**	**C8**	**C12**	**C6/2**	**C7/6**
0.11	n.s.	--	n.s.	--
0.22	n.s.	n.s.	n.s.	n.s.
0.28	n.s.; n.s.	n.s.	n.s.; 27 (0.11)	n.s.; 6 (56)
0.36	n.s.; 22 (0.15)	n.s.	2.5 (0.11); 4 (0.13)	13 (52); 5 (10)
0.43	13 (0.09); 31	1 (0.16); n.s.	< 0.2; 2.2	10 (58); 1 (14)
0.54	s.; 0.6	0.4 (0.17); 55.8 (0.12)	s.; s.	2 (23); < 0.1 (6)
0.65	s.; s.	< 0.1; 5.9	s.	< 0.1 (5); < 0.1 (4)
0.758	s.	s.; s.	s.	< 0.1 (3.5); < 0.1 (3)
0.87	--	--	--	--
1	--	--	--	--

Table S4. Van der Waals (vdW) and electrostatic (elec) energies (kcal/mol) per one BTA molecule averaged over 10 ns (1000 frames) before the field was applied.

SINGLE STACK	**vdW**	**elec**	**total**
C8	-38.58	-52.37	-90.95
C12	-52.43	-58.55	-110.98
C6/2	-38.33	-80.25	-118.58
C7/6	-59.28	-53.05	-112.33
BOX OF 9 STACKS			
C8	-51.29	-50.78	-102.07
C6/2	-53.38	-80.01	-133.39

Table S5. Starting (initiation) time in nanoseconds of the switch for different electric field strengths for individual stack in the box from two independent simulations (given in separate lines). n.s. – non-switching, s. – switching immediately. Min* (max*) value corresponds to the shortest (longest) time needed for the *full switch* of one stack in the box. 'Average*' is an average full switching time of all 9 stacks.

E **(V/nm)**	**C8**	**C6/2**
0.28	n.s.; n.s.; 10; n.s.; n.s.; 27.2; n.s.; n.s.; n.s.	n.s.; n.s.; n.s.; n.s.; n.s.; n.s.; n.s.; 49; n.s. n.s.; n.s.; n.s.; n.s.; n.s.; 14.9; 13.1; n.s.; n.s.
0.36	34.8; 45; n.s.; 2.3; n.s.; n.s.; n.s.; 13.3; 55 1.2; 60; n.s.; n.s.; 2.2; 36; n.s.; n.s.; 17.3	69; n.s.; 59; 11.1; 15.5; n.s.; 2.4; n.s.; 3.8 17.9; 2.8; 32; 14.4; n.s.; n.s.; n.s.; n.s.; 2.5
0.43	35; 46; 4.5; 1; n.s.; 5.6; n.s., 25; 40.8 s.; 7; 13.5; n.s.; >0.2; 8; n.s.; 14.7; 12.4	0.7; 30; 5.5; 3.4; 7.5; 5.6; 1.7; 9.3; 1.5 0.3; 0.1; 1.1; 9.9; 3.3; 1.5; 4; 3; 1.5
0.54	13.4; 5.5; 1.5; 0.2; 3.7; 28, 55; 8; 7.3 1.2; 5; 3.4; 4; s.; 1.8; 2.3; 2.1; 3.3	0.3; 1; 1.3; 1; 1.2; 4.3; 1.4; 2.3; 0.3 0.3; s.; 2.3; 1.2; 0.3; 0.6; 1.2; 0.7; s.
0.65	1; 3; 6; s.; 4; 1.7; s.; 2.9; 4.5 >0.2; >0.2; 1.1; 4; s.; 0.5; s.; 0.7, 0.3	0.3; s.; 0.2; 0.6; 0.2; s.; 1.1; s.; s.
Min*	0.21	0.18
Max*	1.4	1.91
Average*	0.62	0.55

VIII. Figures

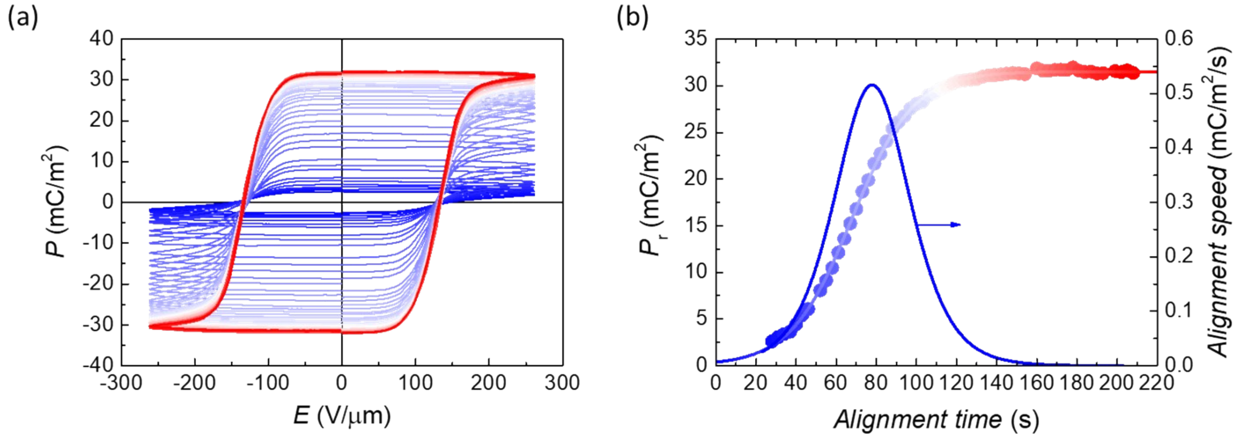

Figure S0. The field-annealing procedure for homeotropic alignment of BTA-C6/2 material at 100°C, 10 Hz. (a) *P-E* hysteresis loops with the remnant polarization growing in cumulative Gaussian fashion with time, see panel (b). The alignment speed increases with applied field, its frequency and temperature.

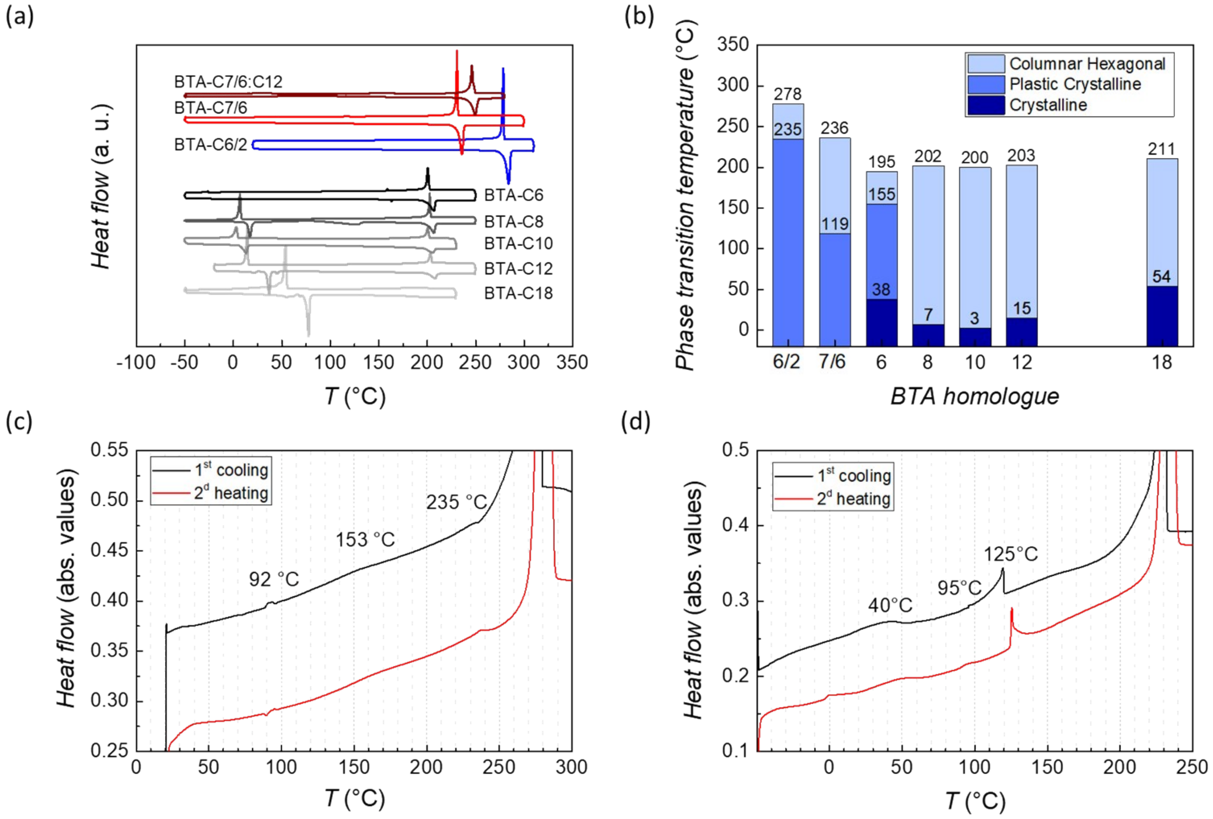

Fig. S1. (a) Differential scanning calorimetry (DSC) thermograms of linear and branched BTAs and a 1:1 BTA-C7/6:C12 blend. The loops are shifted at the ordinate axis for clarity. (b) Phase diagram of different BTA homologues (phase transition temperature values given were measured upon cooling). (c) DSC curves (absolute values) of **BTA-C6/2** material, showing indistinct peaks around 92, 153, 235°C and (d) of **BTA-C7/6** material, with small peaks around 40, 95, 125°C.

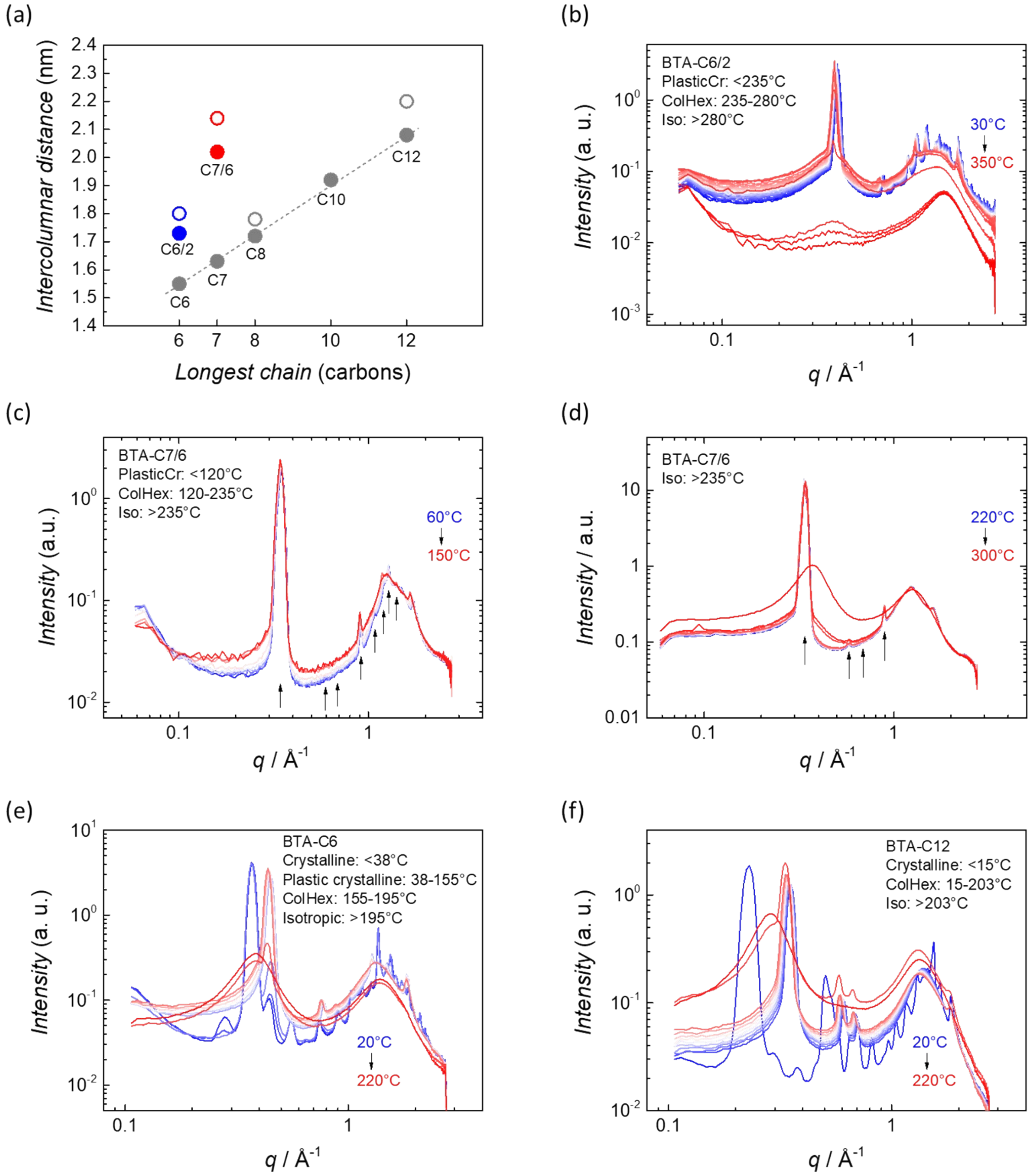

Fig. S2. (a) Experimentally obtained (full circles) and simulated (open circles) intercolumnar distance *a* of a columnar hexagonal lattice for BTA homologues at 353 K and 300 K, respectively.[1] (b) Wide angle X-ray scattering (WAXS) diffractograms at different temperature of **BTA-C6/2** material, showing the typical columnar hexagonal packing pattern below the isotropic temperature 280°C and a plastic crystalline (pseudo-hexagonal) packing below 235°C. (c,d) A temperature scan of WAXS diffractograms for **BTA-C7/6**. Below the isotropic temperature 235°C the material has columnar-hexagonal lattice, yet higher level of order below 120°C indicates plastic-crystalline phase (Bragg peak distance $\sim 1:\sqrt{3}:\sqrt{4}:\sqrt{7}:\sqrt{9}:\sqrt{12}:\sqrt{13}$). No change in XRD diffractograms is seen around 95°C. (e,f) Data for linear BTA-C6 and BTA-C12. WAXS diffractograms for other linear homologues can be found in Ref.[1].

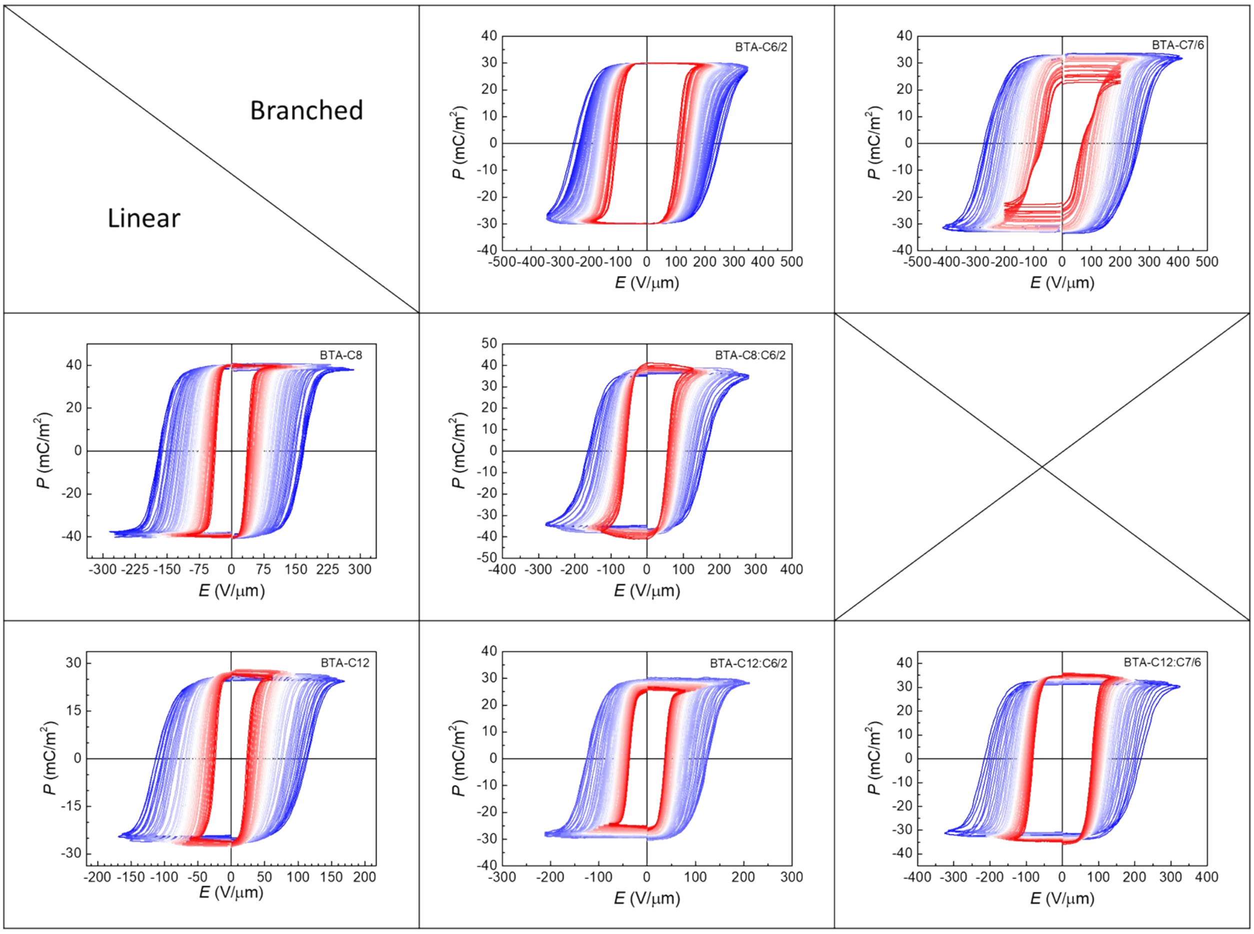

Figure S3. Temperature dependence of the *P*-*E* characteristics (*f* = 10 Hz, *T* = 20–120°C (blue to red)) of linear (**C8**, **C12**), branched (**C6/2, C7/6**) BTAs and 1:1 mixtures of the two (**C8:C6/2**, **C12:C6/2**, **C12:C7/6**). The remnant polarization is essentially temperature independent, while the coercive field follows a mostly linear trend, as described by Equation 1 in the main text.

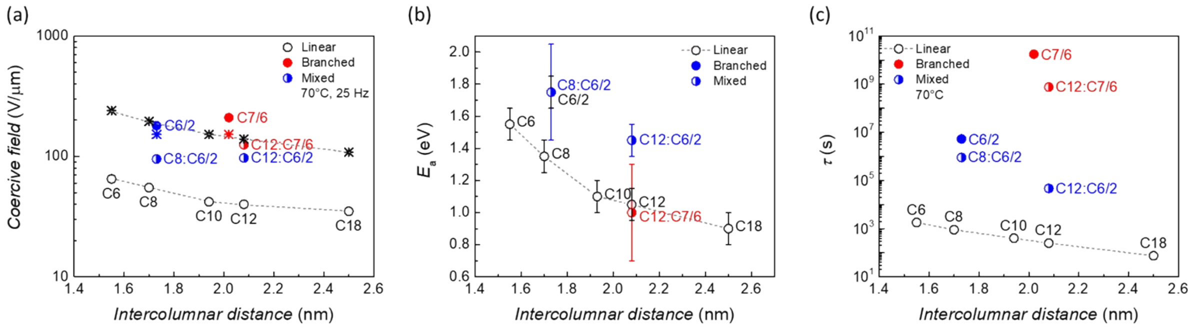

Fig. S4. (a) Experimental coercive field at 70°C and 25 Hz (circles) and intrinsic calculated value based on the Landau-Ginzburg-Devonshire formalism (asterisks), (b) depolarization activation energy and (c) polarization retention at 70°C for linear, branched and mixed materials (as labeled), plotted versus intercolumnar packing distance *a* (measured by WAXS at 80°C). Significant differences between linear and branched-tailed material characteristics with the same packing parameters prove that dipole density is not the only property-determining factor.

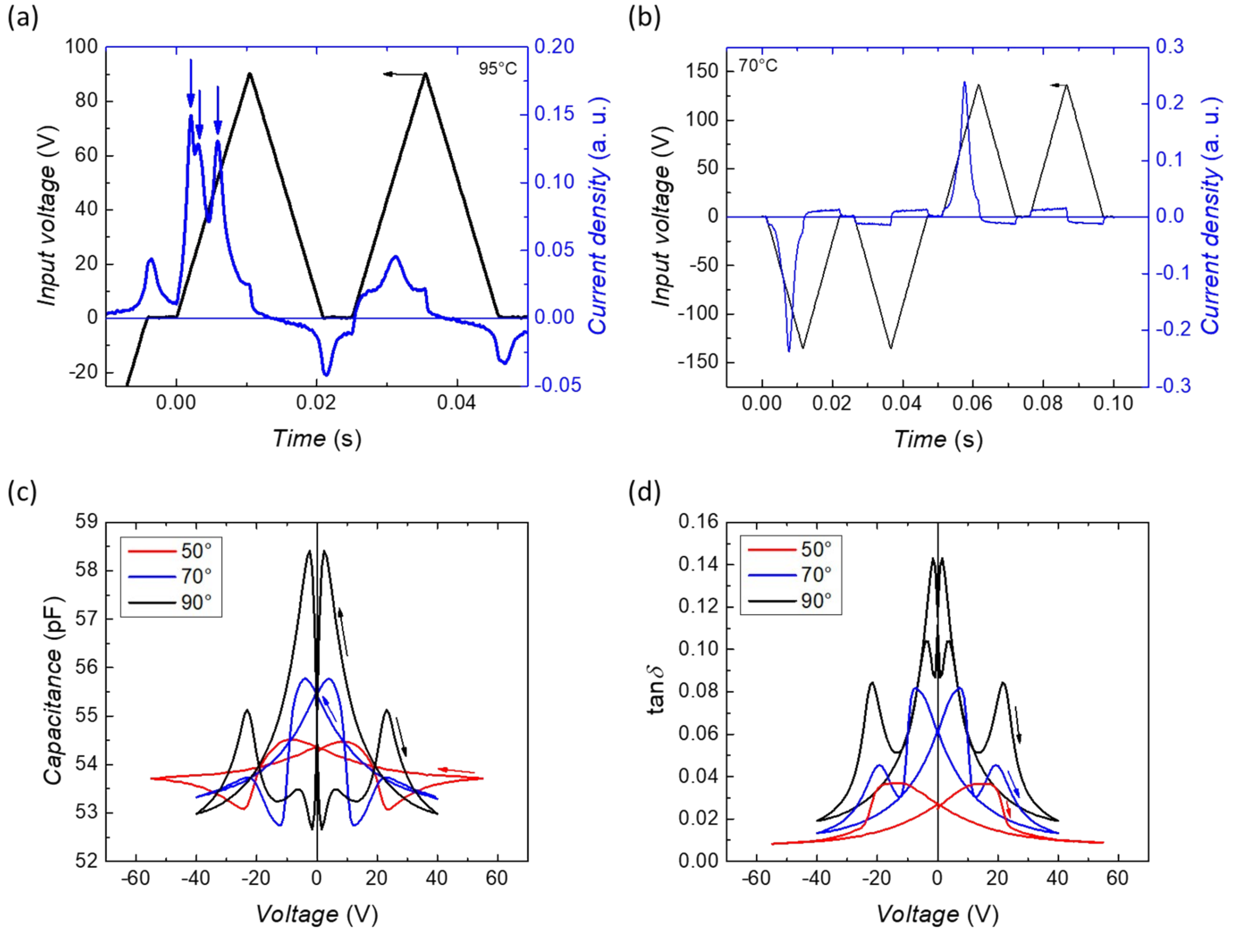

Figure S5. (a,b) Switching current response to a triangular signal for **BTA-C7/6**. Around 90°C and above (panel (a)) three peaks are seen: two of them likely indicate ferrielectric switching, while the third is switching of the lost polarization part during the waiting time between the triangular pulses (seen as a current peak in the opposite direction when the input voltage is 0). The peak appears separately at the second probing pulse (i.e. non-switching current probing). The fact that only one peak appears there denotes that one of the two ferrielectric states is more stable. Below 90°C **BTA-C7/6** has a regular Gaussian ferroelectric switching current peak, see panel (b). A similar trend is seen in (c) small signal capacitance and (d) loss tangent measured at different temperature on **BTA-C7/6** devices. Above 90°C two peaks and immediate polarization relaxation is observed, with high dielectric losses at low voltage range. Below this transition temperature the relaxation is suppressed and **BTA-C7/6** behaves as a regular ferroelectric with *de-facto* no depolarization.

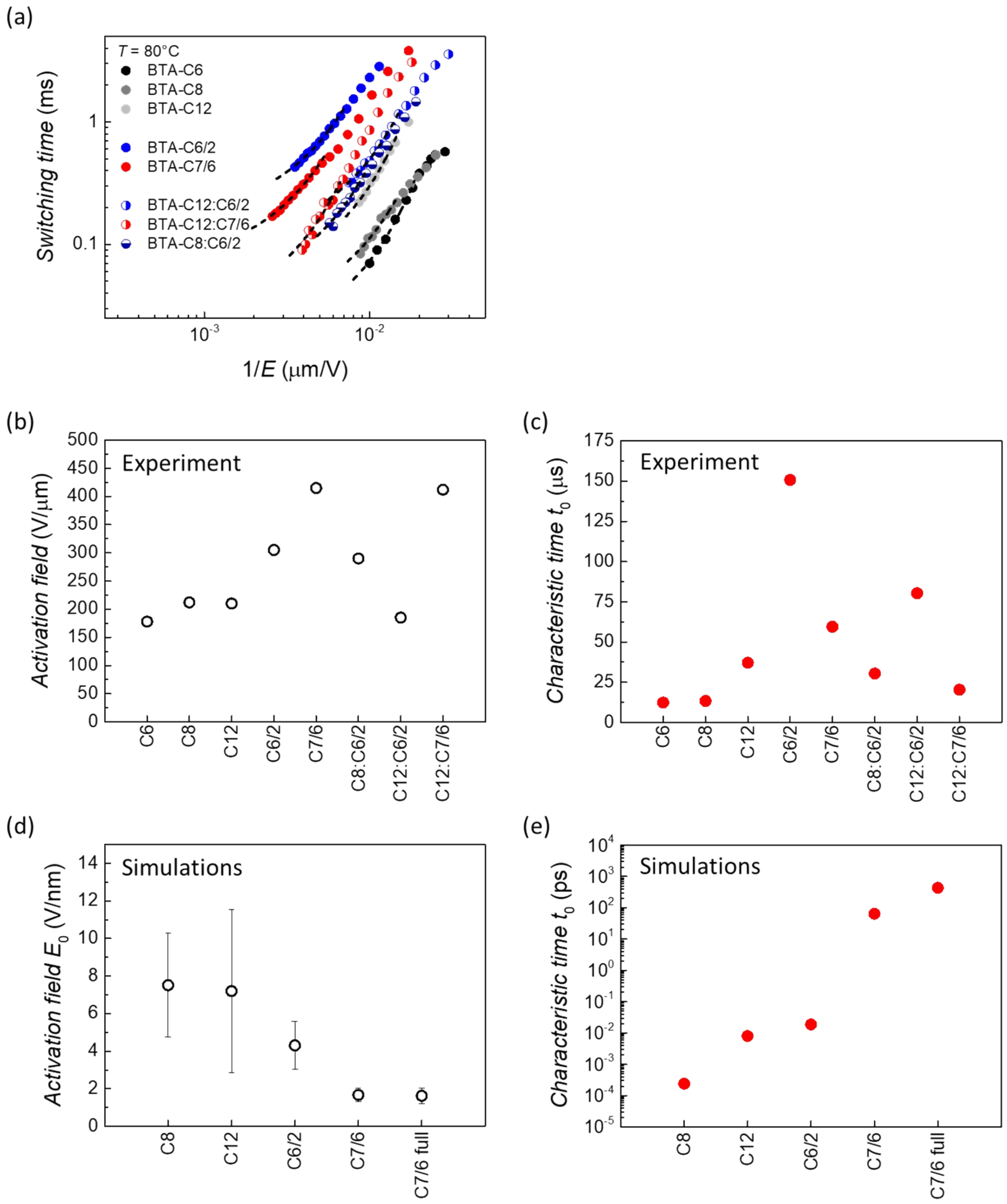

Figure S6. (a) Switching time versus the reciprocal applied field measured at 80°C for different BTA homologues and their mixtures. (b) Activation field E_0 and (c) characteristic minimum switching time t_0 obtained from fitting the experimental high-field data to the Merz equation (dashed black lines in panel (a)). (d,e) Parameters E_0 and t_0, respectively, used to fit the simulated switching initiation time versus applied field trends of a single isolated stack of **BTA-C8**, **C12**, **C6/2** and **C7/6** (Fig. 5b of the main text) to the Merz law: $t_{sw} = t_0 \exp(E_0/E)$. A full switching time is given for **BTA-C7/6** due to exceptionally long polarization switching, compared to <0.2 ns for other homologues.

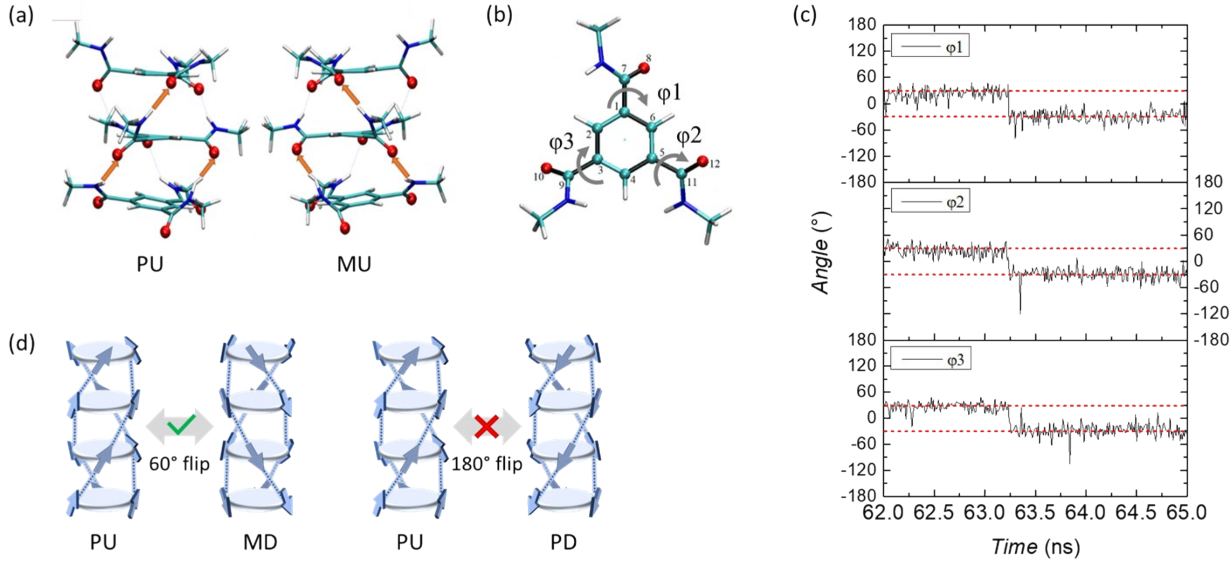

Figure S7. (a) P-helical (left) and M-helical (right) **BTA-C1** with polarization vector pointing up. (b) Dihedral angles φ1, φ2, and φ3. (c) Simulated kinetics of these dihedral angles for the 3:0 rotamer of compound **BTA-C1** at the applied electric field of $E = 0.22$ V/nm in (−)-direction with respect to the z-axis. (d) Polarization flip with a change in helical handedness of the H-bonded microdipole network is preferred: 60° flip (e.g. 30° to −30°) is more energetically favorable than helicity-maintaining 180° flip. P, M denote 'plus' and 'minus' helicity; U, D indicate macrodipole direction 'up' and 'down'.

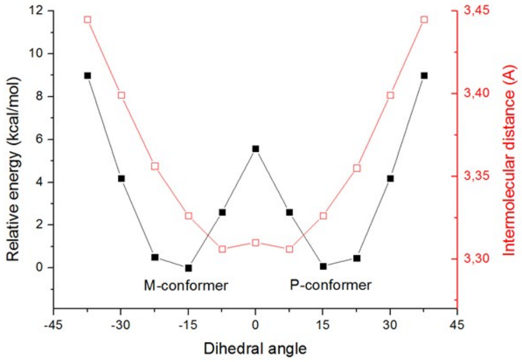

Figure S8. Energy profile determined at B3LYP-D3/cc-pVDZ level of theory. Intermolecular distance is calculated between the phenyl moieties of **BTA-C1** dimer.

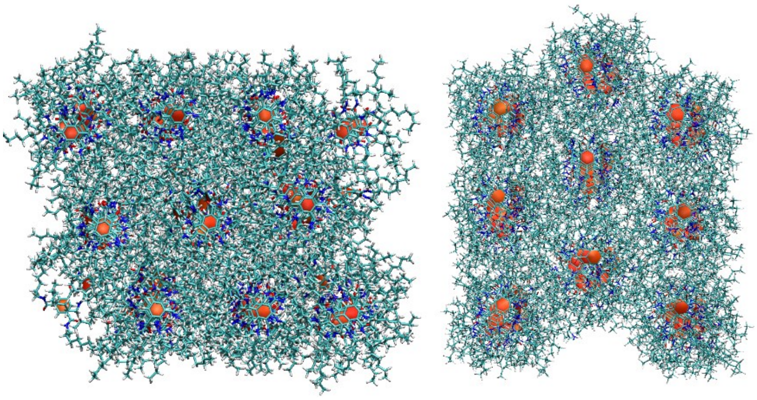

Figure S9. Top view of the box of 9 stacks of compound **C8** (left), and **C6/2** (right). Benzene cores are shown in red.

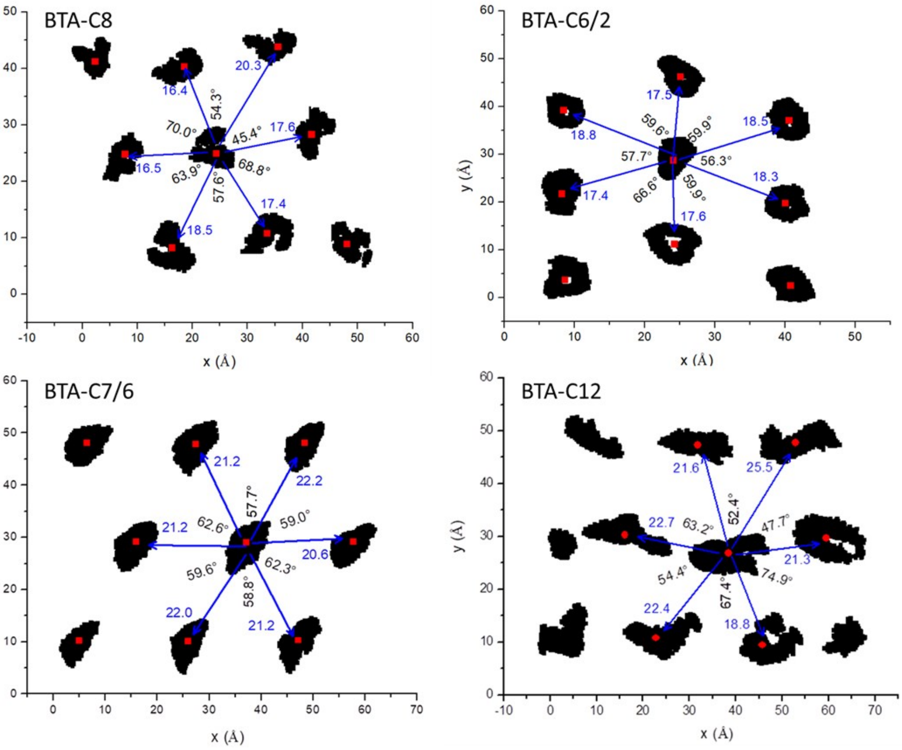

Figure S10. Projection of 100 frames (1 ns) of mass centers of benzene rings of compound **C8**, **C6/2**, **C7/6** and **C12** on the *xy* plane. The hexagon's parameters (in blue) are calculated between the red points that correspond to the average of the corresponding black points.

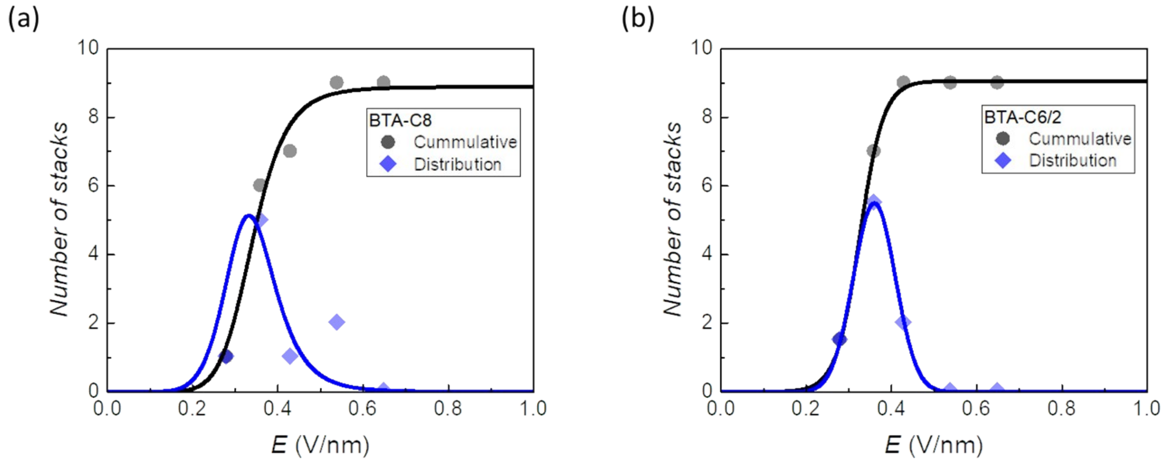

Figure S11. Statistics on the critical switching field (corresponding to the Preisach distribution[16]) of individual stacks in a 9-stack box of **BTA-C8** (a) and **C6/2** (b), showing Gaussian distribution.

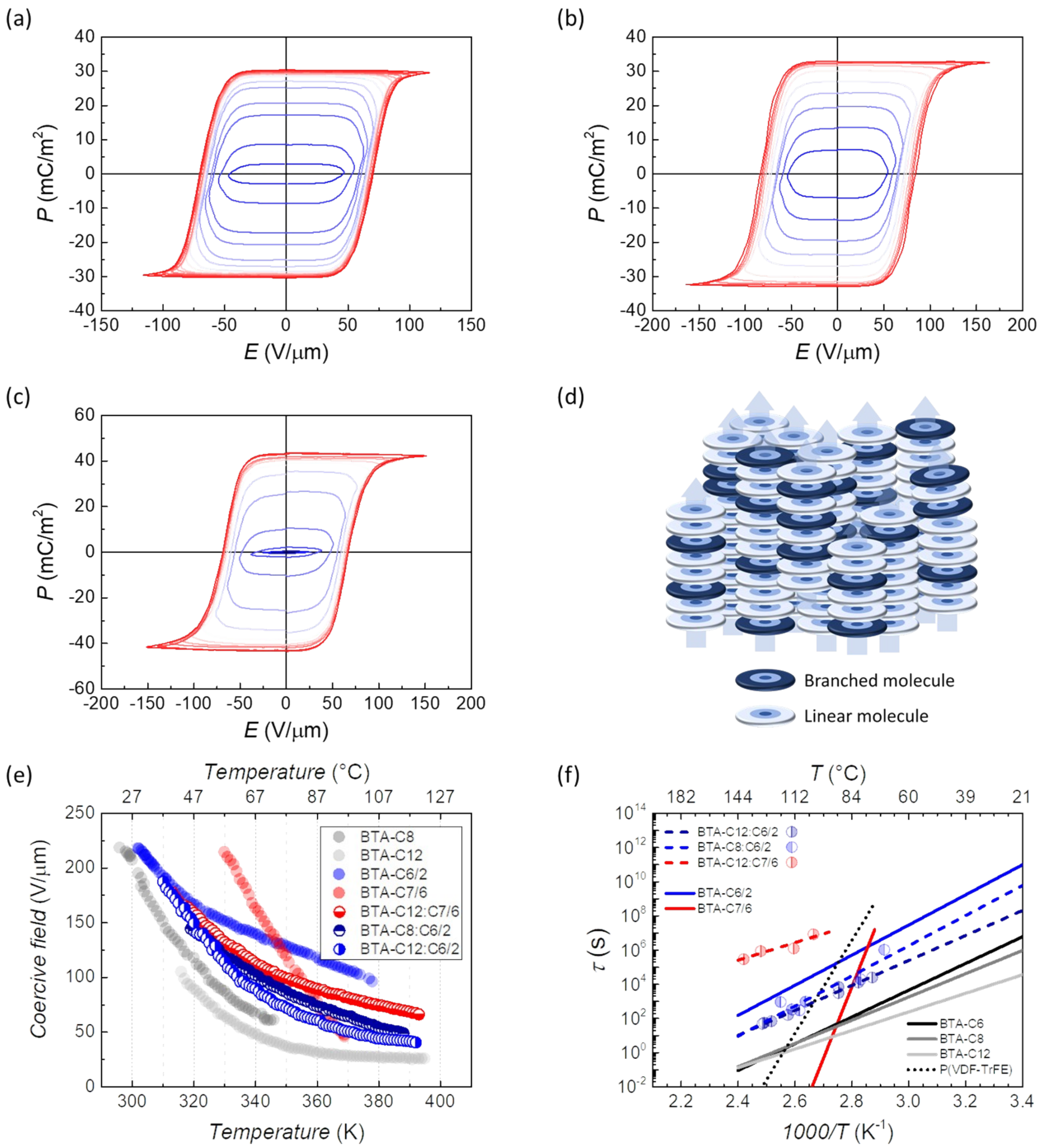

Figure S12. Characteristics of linear-branched BTA mixtures. Polarization hysteresis loops (with inner unsaturated loops) for (a) **BTA-C12:C7/6**, (b) **BTA-C12:C6/2** and (c) **BTA-C8:C6/2**. (d) Illustration of proposed microstructure of intermixed branched and linear molecules within molecular stacks, arrows indicating the direction of the columnar macrodipole. (e) Coercive field *vs.* temperature at 10 Hz field frequency and (f) depolarization activation plot with lines showing fits to the Arrhenius formula (datapoints for pure linear and branched homologues can be found in Fig. 3b of the main text).

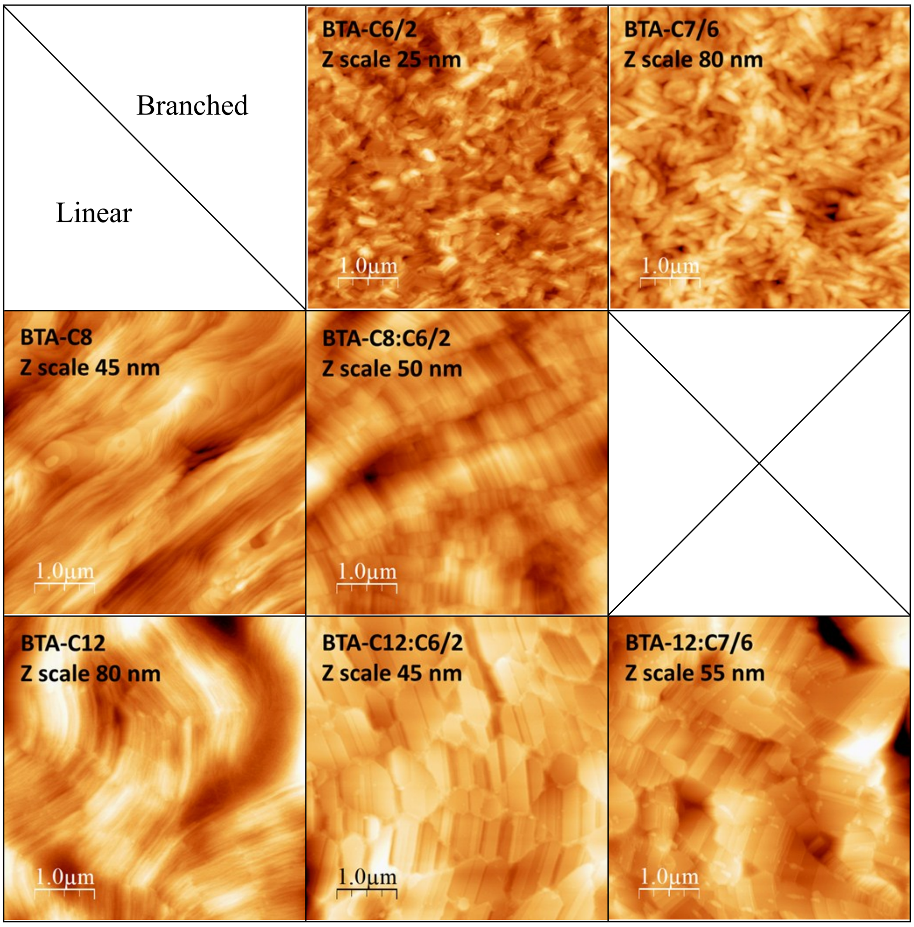

Figure S13. AFM micrographs (height data, 5×5 µm^2, *z* scale given as insets) of spin-coated layers of different BTA homologues, as indicated. Shorter, smaller features are characteristic to branched BTAs **C7/6** and **C6/2** and consist of crystallized molecular stacks. Surface topography of linear BTAs **C8** and **C12** is smoother, with prominent long supramolecular structures. The differences can be attributed to the fact that linear BTAs are still liquid-crystalline, while branched BTAs are plastic-crystalline at room temperature. This may underly more 'linear BTA-like' topography of 1:1 mixtures of linear-branched mixture layers with medium-sized orderly directional structures. Data was obtained in a tapping mode at room temperature on annealed non-aligned (self-assembled) spin-coated layers on glass.

References

1. Urbanaviciute, I. *et al.* Tuning the Ferroelectric Properties of Trialkylbenzene-1,3,5-tricarboxamide (BTA). *Adv. Electron. Mater.* **3,** 1600530 (2017).

2. Fitié, C. F. C., Roelofs, W. S. C., Kemerink, M. & Sijbesma, R. P. Remnant polarization in thin films from a columnar liquid crystal. *J. Am. Chem. Soc.* **132,** 6892–6893 (2010).

3. Fitié, C. F. C. *et al.* Polar switching in trialkylbenzene-1,3,5-tricarboxamides. *J. Phys. Chem. B* **116,** 3928–3937 (2012).

4. Gorbunov, A. V. *et al.* Polarization loss in the organic ferroelectric trialkylbenzene-1,3,5-tricarboxamide (BTA). *Phys. Chem. Chem. Phys.* **19,** 3192–3200 (2017).

5. Gorbunov, A. V. *et al.* True ferroelectric switching in thin films of trialkylbenzene-1,3,5-tricarboxamide (BTA). *Phys. Chem. Chem. Phys.* **18,** 23663–23672 (2016).

6. Kulkarni, C., Reddy, S. K., George, S. J. & Balasubramanian, S. Cooperativity in the stacking of benzene-1,3,5-tricarboxamide: The role of dispersion. *Chem. Phys. Lett.* **515,** 226–230 (2011).

7. Gaussian 09, Revision D.01, M. J. Frisch, G. W. Trucks, H. B. Schlegel, G. E. Scuseria, M. A. Robb, J. R. Cheeseman *et al.*, Gaussian, Inc., Wallingford CT, 2013.

8. Vanquelef, E. *et al.* R.E.D. Server: a web service for deriving RESP and ESP charges and building force field libraries for new molecules and molecular fragments. *Nucleic Acids Res.* **39,** W511–W517 (2011).

9. Pigache, A., Cieplak, P., Dupradeau, F.-Y. Automatic and highly reproducible RESP and ESP charge derivation: Application to the development of programs RED and X RED. *227th ACS National Meeting*, Anaheim, CA, USA, March 28 - April 1 (2004).

10. Dupradeau, F.-Y. *et al.* The R.E.D. tools: advances in RESP and ESP charge derivation and force field library building. *Phys. Chem. Chem. Phys.* **12,** 7821 (2010).

11. Wang, J., Wolf, R. M., Caldwell, J. W., Kollman, P. A. & Case, D. A. Development and testing of a general amber force field. *J. Comput. Chem.* **25,** 1157–1174 (2004).

12. D.A. Case, V. Babin, J.T. Berryman, R.M. Betz, Q. Cai, D.S. Cerutti, T.E. Cheatham, III,

T.A. Darden, R.E. Duke, H. Gohlke, A.W. Goetz, S. Gusarov, N. Homeyer, P. Janowski, J. Kaus, I. Kolossváry, A. Kovalenko, T.S. Lee, S. LeGrand, T. Luchko, R. Luo, B. Madej, K.M. Merz, F. Paesani, D.R. Roe, A. Roitberg, C. Sagui, R. Salomon-Ferrer, G. Seabra, C.L. Simmerling, W. Smith, J. Swails, R.C. Walker, J. Wang, R.M. Wolf, X. Wu and P.A. Kollman (2014), AMBER 14, University of California, San Francisco.

13. D.A. Case, R.M. Betz, D.S. Cerutti, T.E. Cheatham, III, T.A. Darden, R.E. Duke, T.J. Giese, H. Gohlke, A.W. Goetz, N. Homeyer, S. Izadi, P. Janowski, J. Kaus, A. Kovalenko, T.S. Lee, S. LeGrand, P. Li, C. Lin, T. Luchko, R. Luo, B. Madej, D. Mermelstein, K.M. Merz, G. Monard, H. Nguyen, H.T. Nguyen, I. Omelyan, A. Onufriev, D.R. Roe, A. Roitberg, C. Sagui, C.L. Simmerling, W.M. Botello-Smith, J. Swails, R.C. Walker, J. Wang, R.M. Wolf, X. Wu, L. Xiao and P.A. Kollman (2016), AMBER 2016, University of California, San Francisco.

14. Bejagam, K. K., Kulkarni, C., George, S. J. & Balasubramanian, S. External electric field reverses helical handedness of a supramolecular columnar stack. *Chem. Commun.* **51,** 16049–16052 (2015).

15. Albuquerque, R. Q., Timme, A., Kress, R., Senker, J. & Schmidt, H. W. Theoretical investigation of macrodipoles in supramolecular columnar stackings. *Chem. - A Eur. J.* **19,** 1647–1657 (2013).

16. Urbanaviciute, I., Cornelissen, T. D., Meng, X., Sijbesma, R. P. & Kemerink, M. Physical reality of the Preisach model for organic ferroelectrics. *Nat. Commun.* **9,** 4409 (2018).